FRONTIERS OF PHYSICS

RESEARCH ARTICLE
Volume 19 / Issue 5 / 53203 / 2024

High-mobility spin-polarized two-dimensional electron gas at the interface of $LaTiO_3/SrTiO_3$ (110) heterostructures

Zhao-Cai Wang[1], Zheng-Nan Li[1], Shuang-Shuang Li[1], Weiyao Zhao[2], Ren-Kui Zheng[1,3,†]

1 School of Physics and Materials Science, Nanchang University, Nanchang 330031, China
2 Department of Materials Science & Engineering, Monash University, Clayton VIC 3800, Australia
3 School of Physics and Materials Science, Guangzhou University, Guangzhou 510006, China
Corresponding author. E-mail: †zrk@ustc.edu
Received December 17, 2023; accepted February 21, 2024

ABSTRACT

High-quality antiferromagnetic Mott insulator thin films of $LaTiO_3$ (LTO) were epitaxially grown onto $SrTiO_3$ (STO) (110) substrates using the pulsed laser deposition. The LTO/STO heterostructures are not only highly conducting and ferromagnetic, but also show Kondo effect, Shubnikov–de Haas (SdH) oscillations with a nonzero Berry phase of π, and low-field hysteretic negative magnetoresistance (MR). Angle-dependent SdH oscillations and a calculation of the thickness of the interfacial conducting layer indicate the formation of a 4-nm high mobility two-dimensional electron gas (2DEG) layer at the interface. Moreover, an amazingly large low-field negative MR of ~61.8% is observed at 1.8 K and 200 Oe, which is approximately one to two orders of magnitude larger than those observed in other spin-polarized 2DEG oxide systems. All these results demonstrate that the 2DEG is spin-polarized and the 4-nm interfacial layer is ferromagnetic, which are attributed to the presence of magnetic Ti^{3+} ions due to interfacial oxygen vacancies and the diffusion of La^{3+} ions into the STO substrate. The localized Ti^{3+} magnetic moments couple to high mobility itinerant electrons under magnetic fields, giving rise to the observed low-field MR. Our work demonstrates the great potential of antiferromagnetic titanate oxide interface for designing spin-polarized 2DEG and spintronic devices.

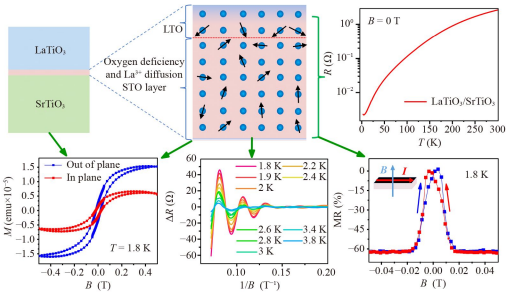

Keywords two-dimensional electron gas, heterostructure, spin polarization, electronic transport, interface

1 Introduction

Perovskite oxide heterostructures have become one of the most interesting materials systems in science and technology. They show a range of fascinating physical properties including high mobility of carriers [1–9], superconductivity [2, 3], ferromagnetism [3], spin–orbit coupling [5], and Shubnikov–de Haas oscillation (SdH) [3]. In complex oxide interface systems such as $LaAlO_3/SrTiO_3$ (LAO/STO), the interfacial ferromagnetism is usually very weak and appears at very low temperatures, and the hysteretic magnetoresistance (MR) also appears at low temperatures (e.g., $T = 0.3$ K) [6]. As of now, a number of interfacial two-dimensional electron gases (2DEG) with spin polarization have been reported [7–9], which offers valuable opportunities to develop oxide-based spintronic devices.

The bulk $LaTiO_3$ (LTO) is an antiferromagnetic Mott insulator with a band gap of 0.2 eV [10]. Metallic

Higher Education Press

https://doi.org/10.1007/s11467-024-1395-6

conductivity can be induced in LTO bulk by transition-metal doping to Ti sites [11] or alkaline-earth doping to La sites [12–14]. Alternatively, metallic conductivity could be realized by depositing LTO thin films on STO (001) substrates to form high mobility 2DEG at the interface of LTO/STO (001) [15–21]. Ohtomo *et al.* [22] experimentally observed charge transfer from LTO to STO and metallic behavior in LTO/STO (001) superlattices. Okamoto *et al.* [23, 24] theoretically proposed that the near-interface region of LTO/STO (001) superlattices is metallic and ferromagnetic due to interface-induced electronic reconstructions, which is later experimentally observed in LTO/STO (001) [15–21]. Recent studies on STO/LTO/STO (001) [25] and LTO/STO/$YTiO_3$/$TbScO_3$ (001) [26] heterostructures show that the (001) interfaces are conducting and weak ferromagnetic. Despite some previous experimental and theoretical efforts on LTO/STO (001) heterostructures, the underlying mechanisms for the interfacial weak ferromagnetism and the evidence for spin polarization of 2DEG are still not well understood and presented. Particularly, the investigation on the possible formation of 2DEG, quantum oscillations, interfacial ferromagnetism, spin polarization, and parameters of Fermi surface of LTO/STO (110) heterostructures are still missing.

On the other hand, for LAO/STO (110) heterostructures, both the STO and LAO can be represented by planar stacks of $(ABO)^{+4}$ and $(O2)^{-4}$ layers. Such a stacking of $(ABO)^{+4}$ and $(O2)^{-4}$ layers will not give rise to polarization discontinuity at the interface [27, 28], and thus no conductivity would be expected for such LAO/STO (110) interfaces. However, 2DEG has been experimentally observed at the LAO/STO (110) interface [29, 30]. Until now, the underlying mechanism for the 2DEG at the (110) interface is still unclear and is less studied for oxide heterostructures.

In this paper, we report the observation of robust spin polarization of high-mobility 2DEG at the interface of a high-quality LTO/STO (110) heterostructure. The interface of the heterostructure is not only high conducting and ferromagnetism but also shows Kondo effect, SdH oscillation with a π Berry phase, and low-field hysteretic negative MR with an amazingly large value of –61.8% at 1.8 K and 200 Oe. Our results show that the 2DEG is spin-polarized and the interface is ferromagnetic. Further, physical parameters of the Fermi surface of the interface were experimentally obtained by analyzing the SdH oscillations.

2 Experimental section

2.1 Sample preparation

LTO films were deposited onto as-received one-side polished 5 mm × 5 mm × 0.5 mm size STO (110) and $(LaAlO_3)_{0.3}(Sr_2AlTaO_6)_{0.7}$ (LSAT) (110) single-crystal substrates by the pulse laser deposition (PLD) using a KrF excimer laser (λ = 248 nm). No additional treatments, such as etching in HF and high temperature annealing, were conducted on the as-received STO substrates. Before deposition, the base pressure of the PLD chamber was evacuated to 5.0×10^{-5} Pa. The working pressure was maintained at 5.0×10^{-4} Pa during the film deposition process. Other preparation parameters such as the target-to-substrate distance, laser energy density, substrate temperature, and pulse repetition rate were kept at 5 cm, 2 J/cm^2, 800 °C, and 6 Hz, respectively. Note that low-temperature (e.g., 500 °C) annealing of the LTO/STO heterostructures in oxygen would convert the LTO film to $La_2Ti_2O_7$ film. Therefore, after the completion of film deposition, the as-grown LTO films were *in-situ* (800 °C, 5.0×10^{-4} Pa) annealed for 30 min and cooled to room temperature at a rate of 10 °C·min^{-1}.

2.2 Structure and valence state characterization

The crystal structure, phase purity, and thickness of LTO films were characterized via X-ray diffraction (XRD) ω, θ–2θ and φ scans, X-ray reflectivity (XRR) as well as the reciprocal space mapping (RSM) using an X-ray diffractometer (SmartLab, Rigaku) equipped with Cu $K_{\alpha 1}$ radiation (λ = 1.5406 Å). Atomic force microscopy (AFM) images were measured using an atomic force microscope (Cypher ES, Oxford Instruments). High-angle annular dark-field scanning transmission electron microscopy (HAADF-STEM) images and electron energy loss spectroscopy (EELS) were measured using a JEM-ARM300F aberration-corrected scanning transmission electron microscope. The specimen for HAADF-STEM measurements were prepared using a FEI Helios 450S dual beam focused ion beam (FIB) system. X-ray photoelectron spectroscopy (XPS) data were collected using an X-ray photoelectron spectrometer (Thermo Scientific K-Alpha). Before XPS measurements, the LTO film was etched by approximately 10 nm along the thickness direction since the surface of the LTO film may be oxidized to $La_2Ti_2O_7$.

2.3 Electronic and magnetic characterization

Electronic characteristics of all thin-film samples were measured with the van der Pauw configuration using a physical property measurement system (PPMS) (DynaCool-14, Quantum Design). Ohmic contacts were prepared on the four corners of each sample using the aluminum (Al) wedge bonding by which the Al wires were directly connected to the interface of heterostructures. The magnetic properties of LTO/STO heterostructures were measured using the superconducting quantum interference device (SQUID) magnetometer (MPMS3, Quantum Design).

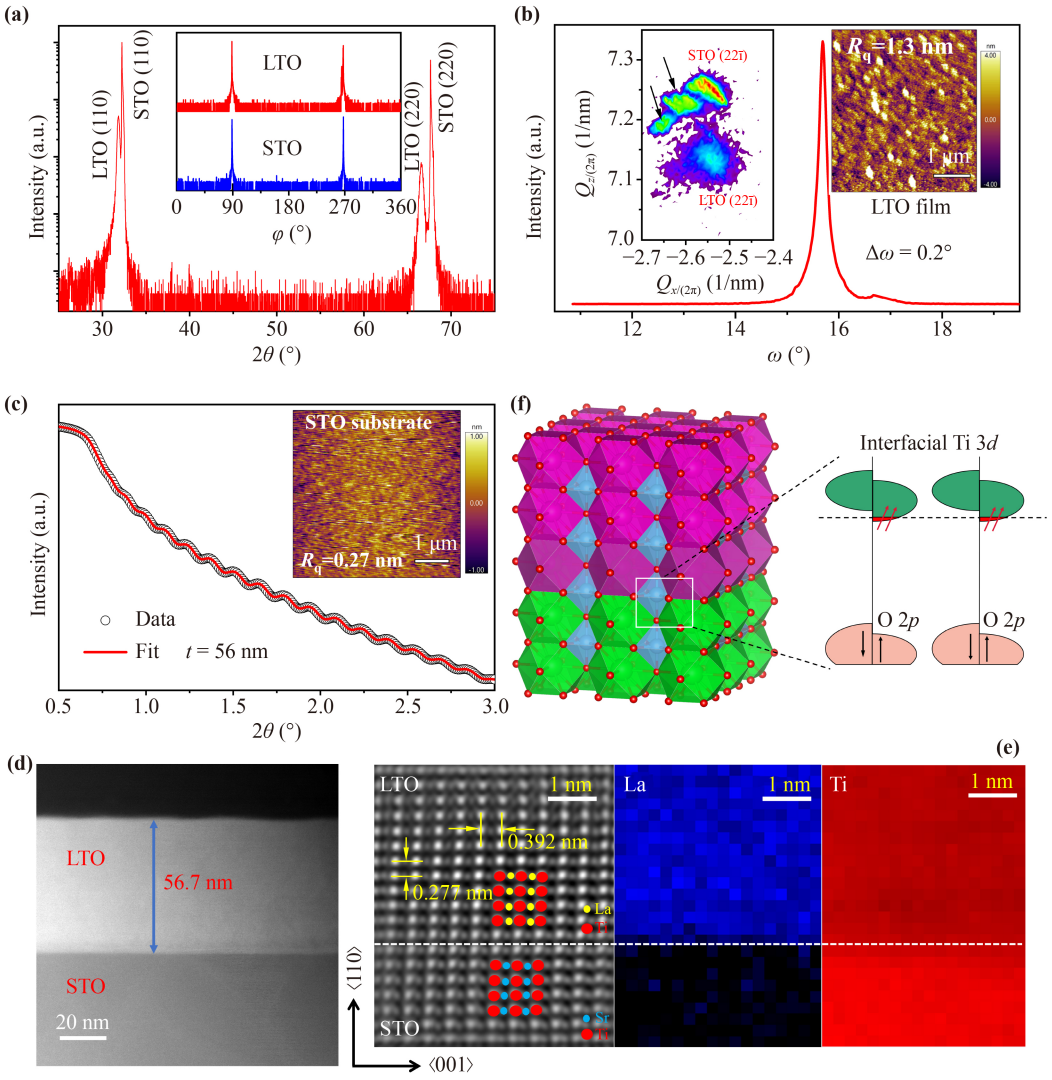

Fig. 1 **(a)** XRD θ–2θ scan pattern for a 56-nm LTO (110) thin film. Inset: φ scan patterns of the LTO film and STO substrate. **(b)** A rocking curve taken on the LTO (110) diffraction peak. Insets: An X-ray RSM pattern and AFM image of the LTO film. **(c)** XRR pattern of the LTO film with theoretical fitting. Inset: AFM image of an as-received STO (110) substrate. **(d)** A TEM image of the LTO/STO heterostructure. **(e)** Left panel: A HAADF-STEM image taken from the interface region. Middle and right panels: EELS mapping of the La and Ti elements. **(f)** Schematic structure of a LTO (110) film on a STO (110) substrate. The red, green, and gray circles are the oxygen, strontium, and titanium atoms, respectively. Right panel: Schematic of the density of states at the interface of the LTO/STO structure with ferromagnetic state.

3 Results and discussion

Figure 1(a) shows the XRD θ–2θ scan pattern of an LTO/STO structure. Only (110) (l = 1, 2) diffraction peaks from the LTO film and STO substrate are observed, indicating that the LTO film is of single phase and highly (110) oriented. XRD φ scans taken on the LTO (111) and STO (111) diffraction peaks yield two sets of two-fold-symmetry diffraction peaks at the same azimuthal angles, as shown in the inset of Fig. 1(a), which reveals that the LTO film has been epitaxially grown on the STO substrate. The XRD ω scan taken on the LTO (110) diffraction peak yields a rocking curve with a full width at half maximum (FWHM) of 0.2° [Fig. 1(b)], implying good crystalline quality of the LTO film. The RSM pattern near STO (22$\bar{1}$) [left inset of Fig. 1(b)] further proves that the LTO film coherently grows on the STO substrate via the cube-on-cube epitaxial mode. Note that the two weaker diffraction spots located at the lower-left positions of the STO (22$\bar{1}$) diffraction spot (as indicated by arrows) arise from the multiple domains of the STO substrate. In Fig. 1(c), the XRR pattern shows Kiessig fringes which result from interference between the reflected X-ray beam from the surface and the one from the film-substrate interface. The film thickness t could be estimated using the equation

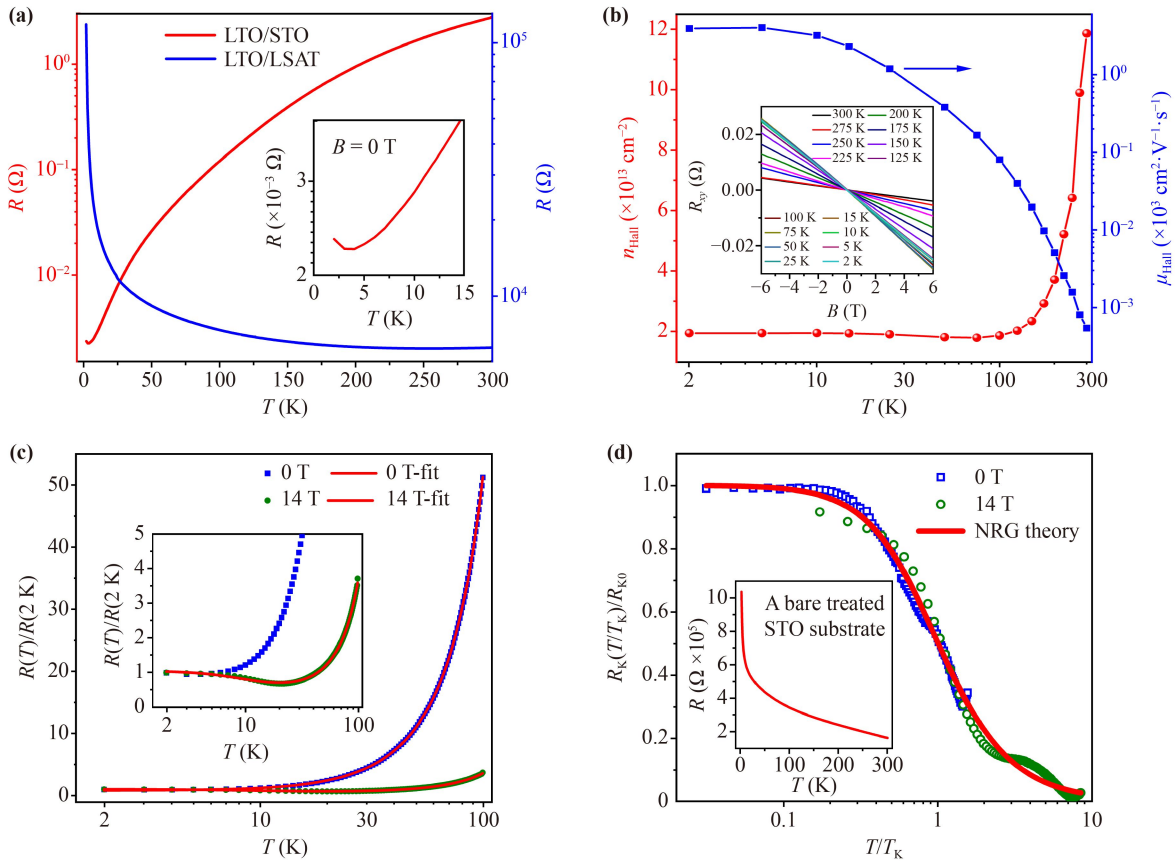

Fig. 2 **(a)** Temperature dependence of the sheet resistance of the LTO/STO (red curve) and LTO/LSAT (blue curve) heterostructures in zero magnetic field. Inset: Magnified view of the resistance upturn at low temperatures. **(b)** Areal carrier density (n_{Hall}) and mobility (μ_{Hall}) derived from Hall measurements as a function of temperature. Inset: Hall resistance R_{xy} as a function of the magnetic field for the LTO/STO heterostructure, as measured at different fixed temperatures. **(c)** Normalized resistance $R(T)/R(2\ \mathrm{K})$ of the LTO/STO structure. Inset: Enlarged view. **(d)** Experimentally (open blue squares and green circles) and theoretically (red curve) scaled Kondo resistance $[R_{\mathrm{K}}(T/T_{\mathrm{K}})/R_{\mathrm{K0}}]$. Inset: Temperature dependence of the resistance of a bare STO substrate that has been treated with the same conditions as those for growing LTO films on STO (110) substrates.

$t = \frac{(m-n)\lambda}{2(\sin\theta_m - \sin\theta_n)}$, where θ_m and θ_n are the diffraction angles of the mth and nth fringes of the XRR pattern, respectively, and λ is the wavelength of the X-ray beam. Using the Rigaku SmartLab Studio software to fit the XRR pattern, the thickness of the LTO film is calculated to be 56 nm, which is well consistent with the thickness measured by a scanning transmission electron microscope (~56.7 nm) [Fig. 1(d)]. The as-grown LTO film has a smooth surface with a root-mean-squared roughness R_{q}~1.3 nm, as demonstrated by the AFM image shown in the right inset of Fig. 1(b). The high-resolution HAADF-STEM image [Fig. 1(e)] reveals the epitaxial growth of the LTO thin film on the STO substrate and smooth of the interface. The EELS show that a very small portion of La^{3+} ions has diffused into the STO substrate side by ~2 nm due to the high substrate temperature during the deposition of films. All these results demonstrate that a high-quality LTO film has been epitaxially grown on the STO (110) substrate. Figure 1(f) displays the schematic of the density of states at the interface of the LTO/STO structure with the ferromagnetic state. The reason for the formation of ferromagnetic state at the LTO/STO interface will be discussed later.

Figure 2(a) shows the temperature dependence of the zero-field resistance for the LTO/STO (red curve) and LTO/LSAT (blue curve) heterostructures. The LTO/STO heterostructure shows metallic conductivity upon cooling from 300 to 4 K and displays a minor resistance upturn below 4 K. It has a high residual resistance ratio ($R_{300\ \mathrm{K}}/R_{1.8\ \mathrm{K}}$) of ~1190, indicating high quality of the LTO/STO heterostructure. In sharp contrast, the simultaneously grown LTO film on the LSAT (110) substrate using the same growth parameters shows insulating behavior, being consistent with that reported in Ref. [48] and the fact that it is a Mott insulator. We also measured the resistance of a bare STO substrate that has been treated with the same conditions as those for

the growth of LTO/STO heterostructures. As shown in the inset of Fig. 2(d), the resistance of such treated STO substrate shows insulating behavior. Therefore, the observed metallic resistance behaviors should only arise from the interface of the LTO/STO heterostructure where electrons accumulate to form a highly conducting interfacial layer. Since we have used as-received STO substrates without surface terrace [inset of Fig. 1(c)], it is highly possible that interfacial electrons are mainly generated by oxygen vacancies rather than electronic reconstruction, similar to the cases of γ-Al_2O_3/$SrTiO_3$ [31] and EuO/$KTaO_3$ [7] systems. This is also consistent with the fact that the LTO films were prepared in a high vacuum environment ($p = 5.0 \times 10^{-4}$ Pa). Using the linear Hall resistance vs. magnetic field data [inset of Fig. 2(b)], the electron mobility and density of the heterostructure are derived and shown in Fig. 2(b). The mobility increases continuously while the carrier density decreases significantly with decreasing temperature from 300 K and appears freezeout, which is a characteristic feature of oxygen deficiency in the surface of STO substrate. As shown in the inset of Fig. 2(a), the sheet resistance of the LTO/STO heterostructure shows slight increase below 4 K. It is noteworthy that the weak localization [32], electron–electron interaction [33], or Kondo effect [6, 34] may give rise to an increase of resistance at low temperatures. Previous studies on the LTO/STO (001) structure have ruled out the weak localization and electron–electron interaction as the origin of the resistance upturn at low temperatures, and attributed the resistance upturn to the Kondo effect [25, 26, 35]. As shown in the inset of Fig. 2(c), upon cooling, the normalized sheet resistance $R(T)/R(2\mathrm{K})$ under $B = 14$ T shows a minimum at 21 K and a pronounced upturn and saturation at lower temperatures. The resistance for both $B = 0$ and 14 T could be quite well fitted using the following Eq. (1) [Fig. 2(c)], which is a characteristic feature of the Kondo effect [25, 26].

As is known, the variation of the resistance with temperature due to the Kondo effect satisfies the universal scaling law [36]. According to the numerical renormalization group (NRG) theory [36–38], the resistance can be expressed by a universal function with a single variable T/T_K:

$$R(T) = R_0 + \alpha T^2 + \beta T^5 + R_\mathrm{K}\left(\frac{T}{T_\mathrm{K}}\right), \tag{1}$$

where

$$R_\mathrm{K}\left(\frac{T}{T_\mathrm{K}}\right) = R_{\mathrm{K}0}\left[\frac{1}{1+\left(2^{1/s}\right)\left(T/T_\mathrm{K}\right)^2}\right]^s, \tag{2}$$

T_K is the Kondo temperature, R_0, αT^2, and βT^5 represent the contributions from the residual resistance, electron–electron interaction, and electron–phonon interaction, respectively, α and β are constants. $R_\mathrm{K}\left(\frac{T}{T_\mathrm{K}}\right)$ is an empirical function for the universal Kondo resistance with respect to the variable T/T_K. $R_{\mathrm{K}0}$ is the Kondo resistance at zero temperature and the parameter s is the effective spin of the magnetic scattering centers. For the LTO/STO (110) system, we take $s = 0.75$ as that was taken in other titanate 2DEG oxide systems [25, 39]. As shown in Fig. 2(d), the renormalized resistances for $B = 0$ and 14 T fall onto a single theoretically calculated curve derived from Eq. (2) (red curve), obeying the universal Kondo scaling. Therefore, the observation of the Kondo effect implies the existence of localized magnetic moments at the interface of the LTO/STO heterostructure, which could couple to high mobility electrons to induce MR in magnetic fields.

Figure 3(a) shows MR vs. B curves of the LTO/STO heterostructure for $B \perp$ film plane at fixed temperatures ranging from 1.8 to 20 K. Here, MR is defined as $\mathrm{MR} = [R(B) - R(0)]/R(0)$, where R_B and R_0 are the resistance in the presence and absence of a magnetic field B, respectively. MR values at different temperatures increase with increasing the magnetic field and there are no signs of saturation up to 14 T. The variation of MR with B follows a quadratic field-dependent behaviors in the –14 T to +14 T region. Interestingly, the low-temperature (1.8–3.8 K) MR vs. B curves show oscillation behaviors in high-field region due to the Landau quantization, namely, the SdH oscillation. After subtracting a smooth polynomial background, the SdH oscillations can be more clearly identified by plotting the oscillation amplitude ΔR against $1/B$ [Fig. 3(b)]. With increasing temperature, ΔR damps gradually. The fast Fourier transform (FFT) spectra of the oscillations are shown in Fig. 3(c), from which the oscillation frequencies (F) are determined to be ~40 T. The oscillatory ΔR can be described by [31, 40]

$$\Delta R = 4R_0 \mathrm{e}^{-\alpha T_D}\alpha T/\sinh(\alpha T), \tag{3}$$

where R_0 is the resistance in zero magnetic field, $\alpha = 2\pi^2 k_B m^*/(e\hbar B_\mathrm{eff})$ and $B_\mathrm{eff} = 2/(1/B_1 + 1/B_2)$ in which B_1 and B_2 are the lower and upper limits of the magnetic field range of the oscillations, respectively, m^* is the ratio of the effective cyclotron mass to the free electron mass m_0, k_B is the Boltzmann constant, $\hbar$ is the reduced Planck constant, and e is the elementary charge. $T_\mathrm{D} = \hbar/(2\pi)k_B\tau$ is the Dingle temperature, where τ is the quantum scattering time. As shown in Fig. 3(d), the normalized FFT amplitude can be well fitted, yielding $m^* = 1.33m_0$. Figure 3(e) shows the Dingle plot of the $\ln[\Delta R\sinh(\alpha T)/(4R_0\alpha T)]$ vs. $1/B$ at a fixed temperature of 1.8 K. Using linear fitting, the obtained slope of which is $-T_D * 2\pi^2 k_B m^*/(e\hbar)$ with $T_D = 2.55$ K, the corresponding τ is 0.476 ps. According to the relation $\mu_\mathrm{SdH} = e\tau/m^*$, the quantum mobility μ_SdH is calculated to be 629 $\mathrm{cm^2{\cdot}V^{-1}{\cdot}s^{-1}}$. Using the Onsager relation of $F = \left(\frac{\varphi_0}{2\pi^2}\right)A_F$, where A_F is the extremal cross-sectional area of the Fermi surface perpendicular to the direction

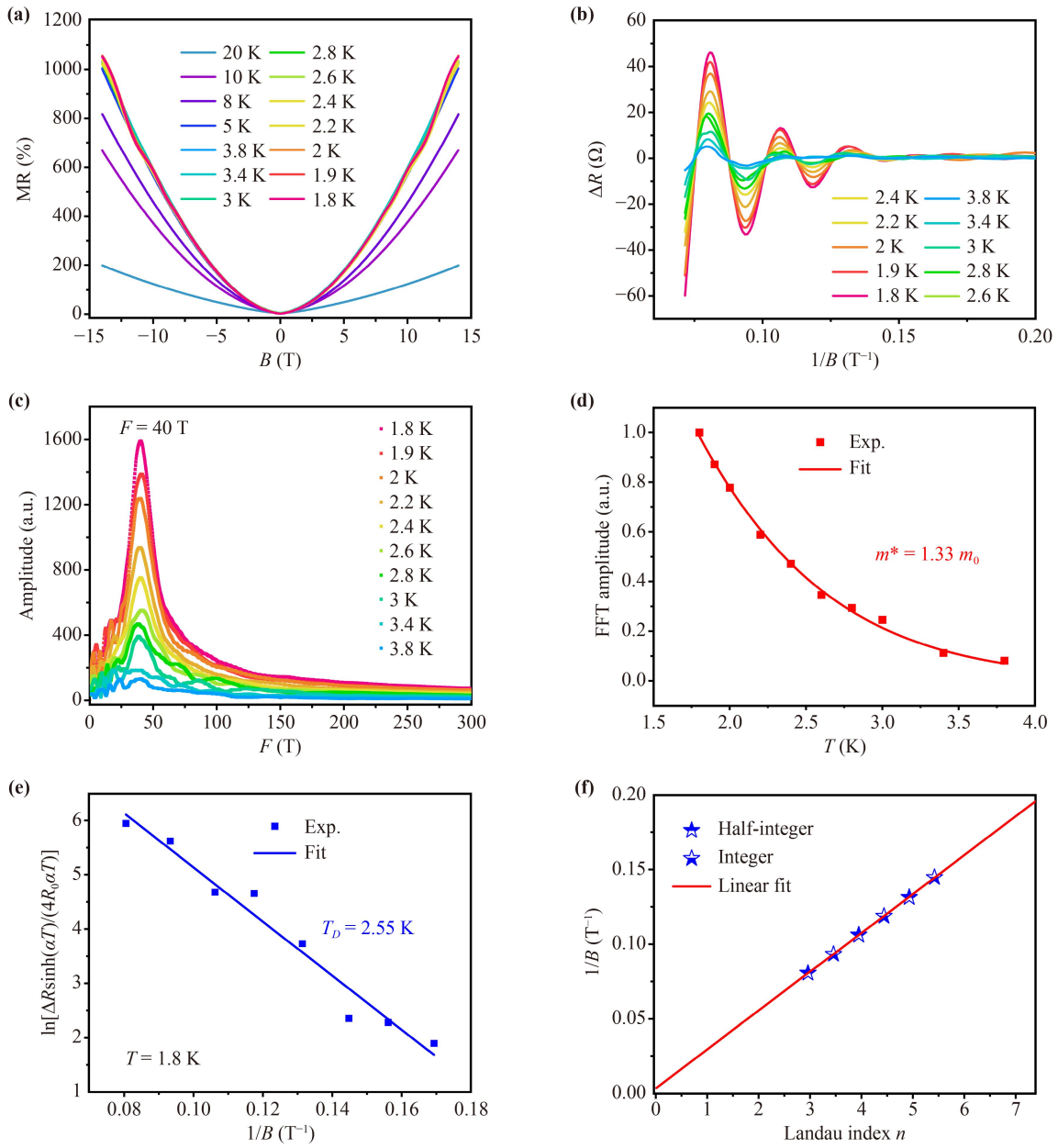

Fig. 3 **(a)** MR vs. B curves at fixed temperatures ranging from 1.8 to 20 K. **(b)** Oscillatory patterns obtained by subtracting a smoothed background. **(c)** The fast Fourier transform (FFT) spectra of the oscillatory patterns. **(d)** Temperature dependence of the normalized FFT amplitude at $F = 40$ T. **(e)** The Dingle plot of the $\ln[\Delta R\sinh(\alpha T)/(4R_0\alpha T)]$ vs. the inverse field $1/B$ at 1.8 K. **(f)** The Landau fan diagram is plotted to illustrate the Berry phase.

of magnetic field, and φ_0 is the magnetic flux quantum, we extract $A_F = 0.038$ Å^{-2}. Using $A_F = \pi k_F^2$, the Fermi wave vectors k_F is calculated to be 0.11 Å^{-1}. Further, using the Luttinger's theorem $n_{2D} = N_v N_s eF/h$, where N_v is the valley degeneracy, N_s is the spin degeneracy, e is the elementary charge, F is the oscillation frequency, and h is Planck's constant, we calculate that n_{SdH} is 1.81×10^{12} cm^{-2} with the choice of $N_v = 1$ and $N_s = 2$. Here, it is noted that the areal carrier density and mobility derived from the SdH oscillations, n_{SdH} (1.81×10^{12} cm^{-2}) and μ_{SdH} (629 cm^2·V^{-1}·s^{-1}), are smaller than those derived from Hall measurements [inset of Fig. 2(b)] ($n_{\mathrm{Hall}} = 1.95 \times 10^{13}$ cm^{-2}, $\mu_{\mathrm{Hall}} = 4 \times 10^3$ cm^2·V^{-1}·s^{-1}), which is consistent with most observations in oxide interfacial systems with 2DEG [36, 41].

SdH oscillation could reveal information about the topology of the electronic band structure and provides insight into the Berry phase of mobile carriers [42]. According to the Lifshitz–Onsager quantization rule, the Berry phase can be derived from the Landau level fan diagram by extrapolating the dependence of $1/B$ on the Landau level index n to $1/B = 0$. The Lifshitz–Onsager

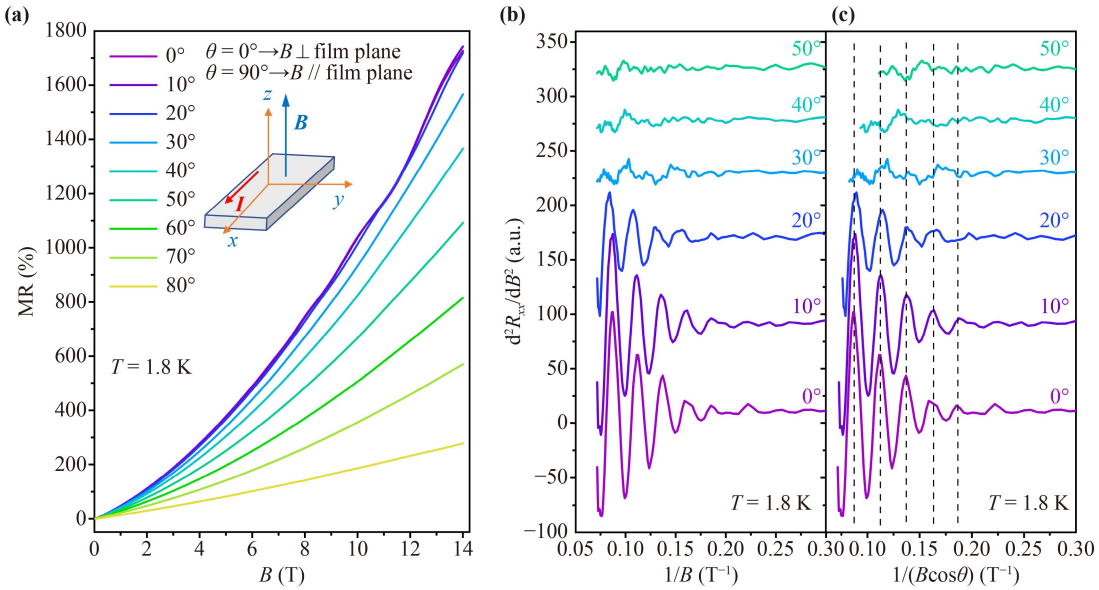

Fig. 4 **(a)** MR as a function of the magnetic field B for different θ angles at $T = 1.8$ K. Inset: schematic illustration of the direction of the magnetic field with respective to the normal of the film plane. **(b)** Second derivative of R_{xx} with respective to B ($\mathrm{d}^2R_{xx}/\mathrm{d}B^2$) plotted against $1/B$. **(c)** $\mathrm{d}^2R_{xx}/\mathrm{d}B^2$ plotted against $1/(B\cos\theta)$.

quantization rule is expressed as

$$A_F\frac{\hbar}{eB} = 2\pi\left(n + \frac{1}{2} - \frac{\phi_B}{2\pi}\right), \tag{4}$$

where ϕ_B is the Berry phase of the orbit in k space. The integer and half-integer indices refer to the peak and valley of the ΔR vs. $1/B$ curves shown in Fig. 3(b). As shown in Fig. 3(f), the intercept of the best linear fit of $1/B$ vs. n for both integer and half-integer indices is practically zero. Therefore, a nonzero Berry phase of π is obtained. Previous reports show that SdH oscillations can only be observed in the LTO/STO (001) structure with the thickness of LTO films less than 10 monolayers (~4 nm) [25], and SdH oscillations disappear when the thickness of the LTO layer is larger than 10 monolayers [25]. It is interesting that SdH oscillations and a nonzero Berry phase of π have been observed in the present LTO/STO (110) heterostructure with a film thickness (56 nm) much larger than 10 monolayers. As is known, the inversion asymmetry at heterostructure interface would naturally induce Rashba-type splitting [25, 43]. As a result, the doubly degenerate Ti t_{2g} energy band are split, leading to the band crossing at the Γ point of the electronic band structure [25]. This, together with the anti-parallel spin characteristics, could induce a Berry curvature in the momentum space, resulting in the nonzero Berry phase of the mobile carriers [25, 43].

To understand the geometry of the Fermi surface, we performed angle-dependent SdH oscillation measurements, as schematically shown in the inset of Fig. 4(a). During the rotation of the thin-film sample, the direction of the magnetic field is always perpendicular to the electric current to minimize the influences of the angle difference between the directions of the magnetic field and the electric current. Here, the angle $\theta = 0°$ is defined as the direction of the magnetic field parallel to the normal of the film plane or perpendicular to the film plane. The MR vs. B curves, as measured at different θ angle, are shown in Fig. 4(a). MR shows appreciable oscillations above $B = 8$ T for $\theta \le 20°$. To see the oscillation more clear, we plot the second derivative of MR with respective to B against $1/B$ in Fig. 4(b), in which the angle-dependent SdH oscillations can be clearly resolved. The oscillations are more remarkable in the low-angle region ($\theta \le 20°$). Its amplitude almost disappears for $\theta > 20°$. As shown in Fig. 4(c), the angular dependence of the oscillation frequency follows the cosine rule $F(\theta) = F(0°)/\cos\theta$. The oscillation only depends on the perpendicular component of the magnetic fields. These results demonstrate that the Fermi surface of the LTO/STO heterostructure is basically two-dimensional. To confirm this conclusion, we calculated the thickness of the interfacial conducting layer using $t = h/(e^2 n_F R_s\sqrt{\alpha})$ [44] where h is the Planck constant, e is the electron charge, $n_F = \sqrt{2\pi n_s}$ is the Fermi wave number, n_s is the carrier density, R_s is the sheet resistance, and α is the ratio of perpendicular MR to parallel MR. t is calculated to be 4.0 nm at 1.8 K, which is consistent with reported thicknesses of typical 2DEG at the LAO/STO interface (2–7 nm) [44–46]. Therefore, the electron gas at the LTO/STO (110) interface is essentially two-dimensional.

Next, we show the interesting butterfly-like hysteretic MR behaviors of the LTO/STO heterostructure. Figure 5(a) shows MR vs. B curves at various low temperatures, with the direction of the magnetic field

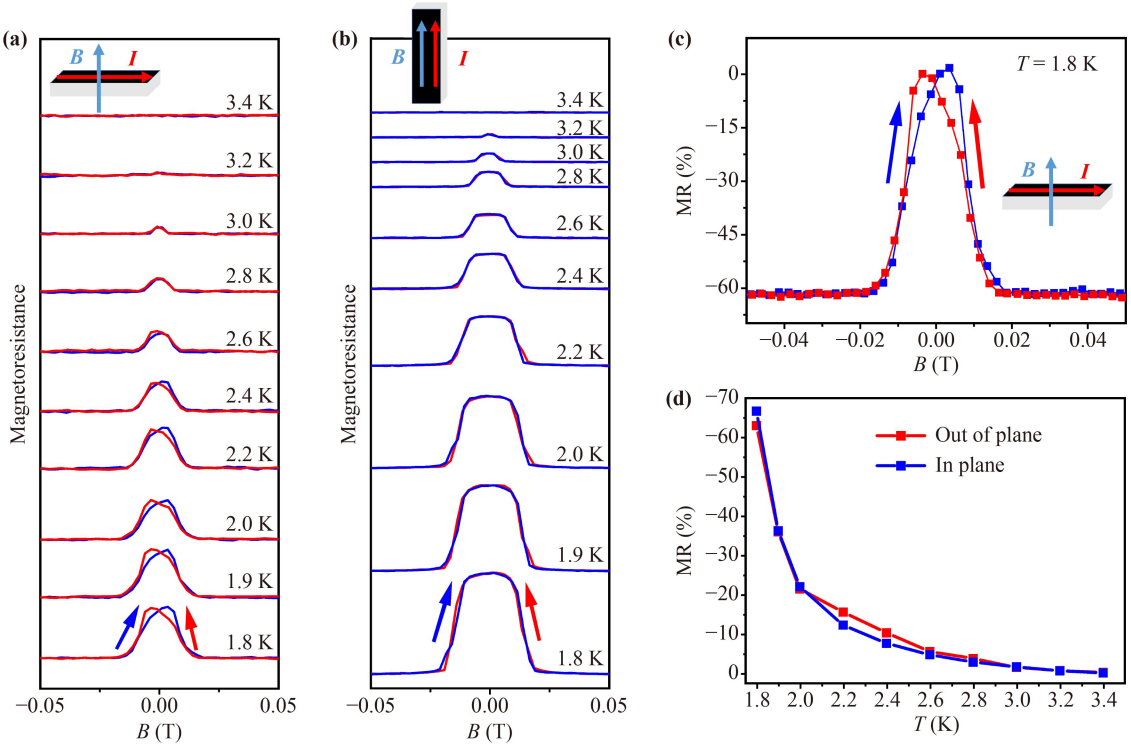

Fig. 5 **(a)** Out-of-plane MR of the LTO/STO heterostructure, as measured at different temperatures with the direction of the magnetic field perpendicular to the film plane. **(b)** In-plane MR of the LTO/STO heterostructure, as measured at different temperatures with the direction of the magnetic field parallel to the film plane and electric current. **(c)** MR vs. B curve at 1.8 K, with the direction of the magnetic field perpendicular to the film plane. **(d)** Out-of-plane and in-plane MR plotted against temperature for $B = 0.05$ T.

perpendicular to film plane [$B\perp$(110) plane]. Amazingly, the MR vs. B curves display butterfly-like shape by sweeping the magnetic field from –0.05 T to 0.05 T to –0.05 T, and moreover, the LTO/STO heterostructure shows low-field negative MR effect, both of which are characteristic signals of ferromagnetic metallic materials. These behaviours survive up to 3.2 K and completely disappear at 3.4 K. The hysteretic low-field MR suggests the existence of ferromagnetic order at the interface of the LTO/STO heterostructure. As shown in Fig. 5(b), the MR vs. B curves for the direction of the magnetic field parallel to the film plane [B//(110) plane] also display butterfly-like shape, however, with weaker hysteretic characteristics. Their variation trend with temperature is similar to that for $B\perp$(110) plane. These results demonstrate that the low-field MR effect is mainly due to the isotropic suppression of magnetic scattering by applied magnetic fields, similar to that observed in isotropic granular ferromagnetic materials [47]. Figure 5(c) shows the enlarged view of the MR vs. B curve at 1.8 K, for $B\perp$(110) plane. The maximal negative MR reaches 61.8% at $B = 200$ Oe and saturated for larger fields. Such a large low-field negative MR is surprising since the negative MR in other spin-polarized 2DEG oxide systems are less than 1%, e.g., MR = 0.8% for LTO/$EuTiO_3$ [48], MR = 0.2% for EuO/$KTaO_3$ [7], MR = 0.3% for STO/LTO [21], and MR = 1% for $NdTiO_3$/STO [49]. Figure 5(d) shows the low-field saturation MR as a function of temperature for both $B\perp$(110) plane (out of plane) and B//(110) plane (in plane). For both configurations, MR almost coincide with each other, implying the negative MR effect is basically isotropic. To further prove that the negative MR arises from the ferromagnetic interfacial layer, we measured the magnetotransport properties of LTO films with similar thickness (~56 nm) grown on the LSAT and $LaAlO_3$ substrates using the same preparation conditions, as shown in Fig. 6. The LTO films grown on LSAT and $LaAlO_3$ substrates show insulating resistance behaviors and positive MR effect without hysteresis at $T = 2$ K, which demonstrates that the observed negative MR in LTO/STO heterostructures is not from LTO film itself. All these results demonstrate that ferromagnetic order has been established at the interface of the LTO/STO heterostructure and the interfacial electron gas is spin-polarized.

Further, temperature-dependent magnetization was measured to understand the magnetic properties of the LTO/STO heterostructure. During the measurements, the zero-field-cooled (ZFC) and field-cooled (FC) magnetization were recorded in the heating process, with a magnetic field of 100 Oe applied perpendicular and

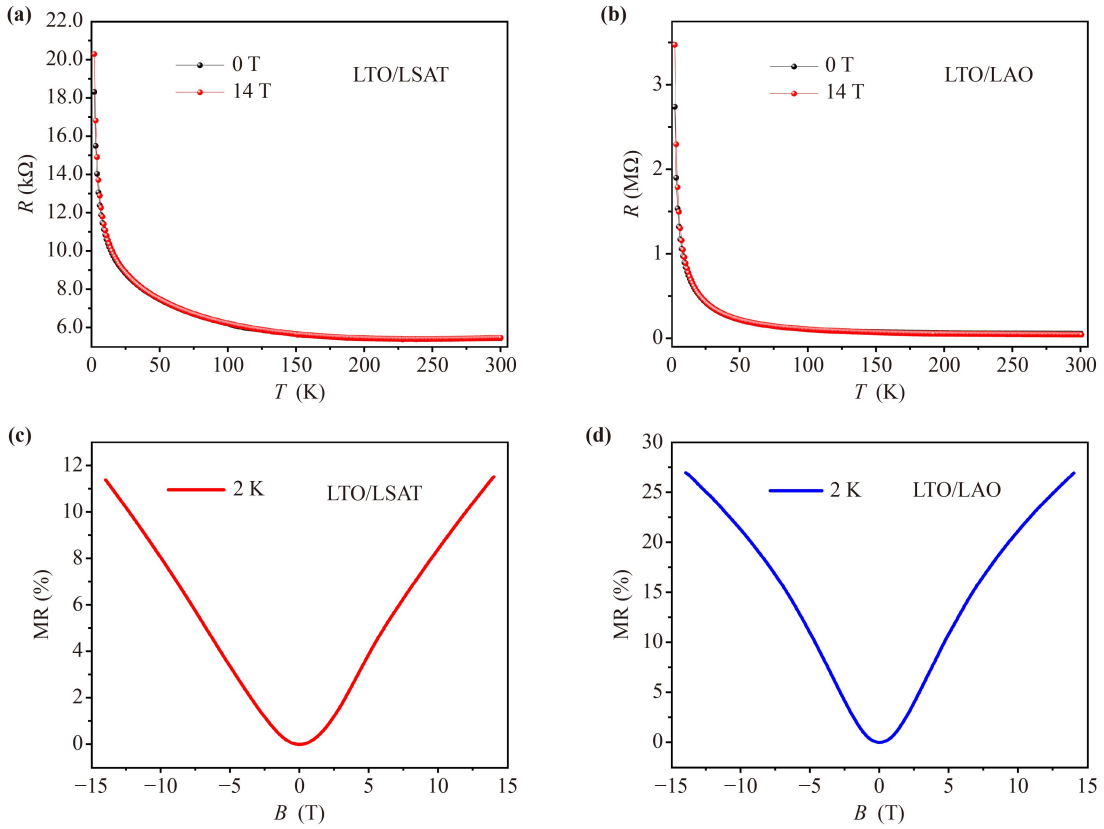

Fig. 6 Temperature dependence of the resistance for **(a)** LTO/LSAT and **(b)** LTO/LAO heterostructures in zero magnetic field and a magnetic field of 14 T, and magnetic field dependence of MR at $T = 2$ K for **(c)** LTO/LSAT and **(d)** LTO/LAO heterostructures.

parallel to the film plane, respectively. Figure 7(a) shows temperature dependence of the out-of-plane and in-plane magnetization. Here, the diamagnetic signals from the STO substrates have been subtracted. For both out-of-plane and in-plane configurations, difference between the ZFC and FC curves can be observed below 275 K, indicating a history-dependence of the magnetization, which is a signature of a magnetically ordered state. Figure 7(b) shows the out-of-plane and in-plane magnetic hysteresis loops at 1.8 K for the LTO/STO heterostructure. The out-of-plane saturation magnetization is larger than those of the in-plane ones, indicating magnetic anisotropy of the LTO/STO heterostructure. This may account for the difference in the shape of the MR vs. B curves in Figs. 5(a) and (b). To qualitatively distinguish the source of the ferromagnetism, we measured the magnetic hysteresis loops of a 56-nm LTO film grown on a LSAT single-crystal substrate and show the results in Fig. 7(d). The LTO/LSAT heterostructure also displays ferromagnetic hysteresis loops, which is due to the presence of Ti^{3+}/Ti^{4+} mixture in LTO film arising from oxygen over-doping [50]. XPS pattern collected from the LTO/STO heterostructure confirms the existence of Ti^{3+} and Ti^{4+} ions in the LTO film, as indicated by Ti valence states near Ti 2p binding energy in Fig. 7(c). A quantitative comparison of the saturation magnetization between LTO/LSAT and LTO/STO heterostructures indicate that both the out-of-plane and in-plane saturation magnetization of the former is much weaker than those of the latter, respectively. This implies that the enhanced saturation magnetization in the LTO/STO heterostructure could be additionally contributed from the interfacial ferromagnetic layer of the heterostructure.

For STO/LTO/STO heterostructures [25], when the thickness of the LTO layer is 2 or 10 monolayers (MLs), there are localized moments at the LTO interfaces, however, when the thickness of the LTO layer is 20 MLs, antiferromagnetic ordering is recovered in the LTO layer. As a result, the STO/LTO (20 MLs)/STO heterostructure shows bulk-like antiferromagnetism. Further, density functional theory calculations conducted on $(STO)_4/(LTO)_6$ superlattices reveal the recovery of antiferromagnetic ordering in the 6-MLs LTO layer [51]. These results demonstrate that LTO films with a thickness larger than 10 MLs are intrinsically antiferromagnetic. Back to our experimental results, the thickness of the LTO film (~56 nm, ~141 MLs) is much larger than the thickness limit for showing ferromagnetism. Therefore, it is believed that the 56-nm LTO film is essentially antiferromagnetic with very weak ferromagnetic signal in the

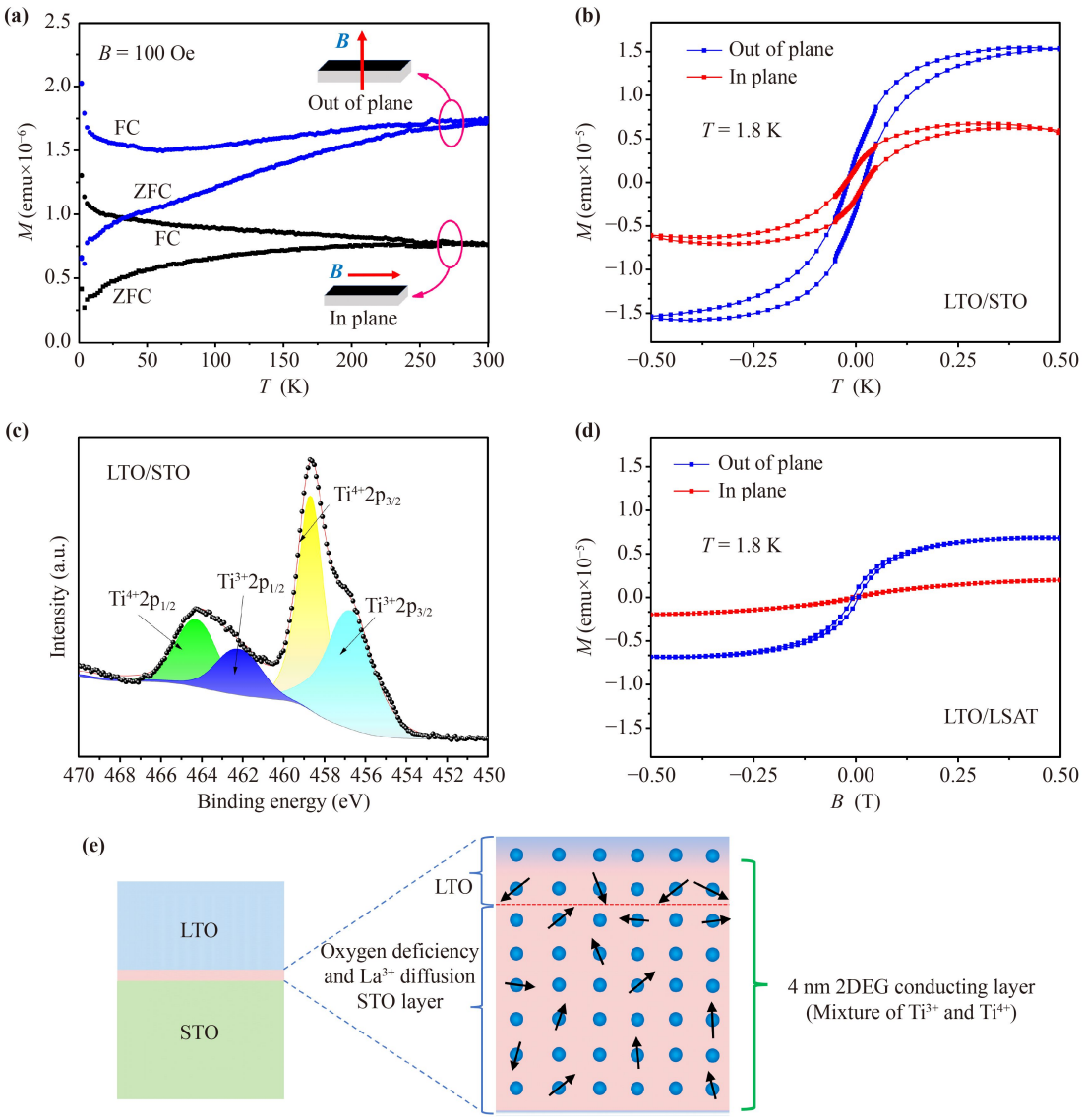

Fig. 7 **(a)** Temperature dependence of the zero-field-cooled (ZFC) and field-cooled (FC) magnetization for the LTO/STO heterostructure, as measured with a magnetic field of 100 Oe applied perpendicular and parallel to the film plane, respectively. **(b)** Out-of-plane and in-plane magnetization vs. magnetic field at 1.8 K for a 56-nm LTO/STO heterostructure. **(c)** XPS spectra around the binding energy of Ti 2p for the LTO film grown on STO (110). **(d)** Out-of-plane and in-plane magnetization vs. magnetic field at 1.8 K for a 56-nm LTO/LSAT heterostructure. **(e)** Schematically illustration of the origin of the interfacial ferromagnetism in the LTO/STO (110) heterostructure.

order of 10^{-6} emu, arising from the presence of Ti^{4+} ions in LTO film due to oxygen over-doping, although there may exist localized moments within one interfacial monolayer neighboring to STO substrate [25]. Although the 56-nm LTO/STO heterostructure show ferromagnetism, we believe that the low-field negative MR (61.8% @1.8 K and 200 Oe) is solely related to the 4-nm interfacial ferromagnetic conducting layer which consists one monolayer of LTO and thin layer of STO, as schematically illustrated in Fig. 7(e). Since the LTO film was deposited onto STO substrate in a high vacuum (5.0×10^{-4} Pa) and high temperature (800 °C) environment, oxygen vacancies would be inevitably generated at the interface of the STO side, resulting in Ti^{3+} ions at the interface. Moreover, the diffusion of a portion of La^{3+} ions into the surface layer of STO would induce additional Ti^{3+} ions at the surface layer (~4 nm). Further, the broken of the inversion symmetry at interface could cause surface layer of Ti^{3+} ions at the LTO side to be ferromagnetic in magnetic fields because of the absence of antiferromagnetic spin coupling. Therefore, all Ti^{3+} moments within the 4-nm conducting layer would be aligned to the magnetic-field direction and couple to high-mobility itinerant electrons, leading to the low-field negative MR.

4 Conclusions

To summarize, we have fabricated high-quality LTO/STO heterostructures by depositing 56-nm LTO thin films onto STO (110) single-crystal substrates by the pulsed laser deposition. Hall and SdH oscillation measurements reveal the formation of high-mobility electron gas with a Berry phase of π at the interface of the heterostructure. Angle-dependent SdH measurements combining with a calculation of the thickness of the interfacial conducting layer (4 nm) reveal that electron gas is essentially two-dimensional. The observed Kondo effect, large low-field hysteretic negative magnetoresistance, and magnetic hysteresis loops strongly demonstrate that the interfacial 2DEG is spin-polarized. The origin of the interfacial ferromagnetism is mainly attributed to the presence of magnetic Ti^{3+} ions at the interface due to oxygen vacancies and the diffusion of La^{3+} ions into STO substrate. Our findings on LTO/STO (110) heterostructures provide a more comprehensive and in-depth understanding of the spin-polarized 2DEG at the antiferromagnetic titanate oxide interface.

Declarations The authors declare that they have no competing interests and there are no conflicts.

Acknowledgements This work was supported by the National Natural Science Foundation of China (Grant No. 11974155), the Natural Science Foundation of Guangdong Province (Grant No. 2022A1515010583), and Bureau of Education of Guangzhou Municipality (Grant No. 202255464).

References

1. A. Ohtomo and H. Y. Hwang, A high-mobility electron gas at the $LaAlO_3/SrTiO_3$ heterointerface, *Nature* 427(6973), 423 (2004)
2. N. Reyren, S. Thiel, A. D. Caviglia, L. F. Kourkoutis, G. Hammerl, C. Richter, C. W. Schneider, T. Kopp, A. S. Ruetschi, D. Jaccard, M. Gabay, D. A. Muller, J. M. Triscone, and J. Mannhart, Superconducting interfaces between insulating oxides, *Science* 317(5842), 1196 (2007)
3. J. A. Bert, B. Kalisky, C. Bell, M. Kim, Y. Hikita, H. Y. Hwang, and K. A. Moler, Direct imaging of the coexistence of ferromagnetism and superconductivity at the $LaAlO_3$ /$SrTiO_3$ interface, *Nat. Phys.* 7(10), 767 (2011)
4. C. Cao, S. G Chen, J. Deng, G. Li, Q. H Zhang, L. Gu, T. P. Ying, E. J. Guo, J. G. Guo, and X. L. Chen, Two-dimensional electron gas with high mobility forming at $BaO/SrTiO_3$ interface, *Chin. Phys. Lett.* 39(4), 047301 (2022)
5. W. M. Jiang, Q Zhao, J. Z. Ling, T. N. Shao, Z. T. Zhang, M. R. Liu, C. L. Yao, Y. J. Qiao, M. H. Chen, X. Y. Chen, R. F. Dou, C. M. Xiong, and J. C. Nie, Gate tunable Rashba spin–orbit coupling at $CaZrO_3$/$SrTiO_3$ heterointerface, *Chin. Phys. B* 31(6), 066801 (2022)
6. A. Brinkman, M. Huijben, M. Van Zalk, J. Huijben, U. Zeitler, J. C. Maan, W. G. Van der Wiel, G. Rijnders, D. H. A. Blank, and H. Hilgenkamp, Magnetic effects at the interface between non-magnetic oxides, *Nat. Mater.* 6(7), 493 (2007)
7. H. R. Zhang, Y. Yun, X. J. Zhang, H. Zhang, Y. Ma, X. Yan, F. Wang, G. Li, R. Li, T. Khan, Y. S. Chen, W. Liu, F. X. Hu, B. G. Liu, B. G. Shen, W. Han, and J. R. Sun, High-mobility spin-polarized two-dimensional electron gases at $EuO/KTaO_3$ interfaces, *Phys. Rev. Lett.* 121(11), 116803 (2018)
8. D. Stornaiuolo, C. Cantoni, G. M. De Luca, R. Di Capua, E. Di. Gennaro, G. Ghiringhelli, B. Jouault, D. Marrè, D. Massarotti, F. Miletto Granozio, I. Pallecchi, C. Piamonteze, S. Rusponi, F. Tafuri, and M. Salluzzo, Tunable spin polarization and superconductivity in engineered oxide interfaces, *Nat. Mater.* 15(3), 278 (2016)
9. D. Stornaiuolo, B. Jouault, E. Di Gennaro, A. Sambri, M. D'Antuono, D. Massarotti, F. M. Granozio, R. Di Capua, G. M. De Luca, G. P. Pepe, F. Tafuri, and M. Salluzzo, Interplay between spin–orbit coupling and ferromagnetism in magnetotransport properties of a spin-polarized oxide two-dimensional electron system, *Phys. Rev. B* 98(7), 075409 (2018)
10. T. Arima, Y. Tokura, and J. B. Torrance, Variation of optical gaps in perovskite-type $3d$ transition-metal oxides, *Phys. Rev. B* 48(23), 17006 (1993)
11. C. Eylem, Y. C. Hung, H. L. Ju, J. Y. Kim, D. C. Green, T. Vogt, J. A. Hriljac, B. W. Eichhorn, R. L. Greene, and L. Salamanca-Riba, Unusual metal–insulator transitions in the $LaTi_{1-x}V_xO_3$ perovskite phases, *Chem. Mater.* 8(2), 418 (1996)
12. Y. Okada, T. Arima, Y. Tokura, C. Murayama, and N. Môri, Doping- and pressure-induced change of electrical and magnetic properties in the Mott–Hubbard insulator $LaTiO_3$, *Phys. Rev. B* 48(13), 9677 (1993)
13. C. C. Hays, J. S. Zhou, J. T. Markert, and J. B. Goodenough, Electronic transition in $La_{1-x}Sr_xTiO_3$, *Phys. Rev. B* 60(14), 10367 (1999)
14. T. Katsufuji, Y. Taguchi, and Y. Tokura, Transport and magnetic properties of a Mott–Hubbard system whose bandwidth and band filling are both controllable: $R_{1-x}Ca_xTiO_{3+y/2}$, *Phys. Rev. B* 56(16), 10145 (1997)
15. F. J. Wong, S. H. Baek, R. V. Chopdekar, V. V. Mehta, H. W. Jang, C. B. Eom, and Y. Suzuki, Metallicity in $LaTiO_3$ thin films induced by lattice deformation, *Phys. Rev. B* 81(16), 161101(R) (2010)
16. C. He, T. D. Sanders, M. T. Gray, F. J. Wong, V. V. Mehta, and Y. Suzuki, Metal–insulator transitions in epitaxial $LaVO_3$ and $LaTiO_3$ films, *Phys. Rev. B* 86(8), 081401(R) (2012)
17. J. Biscaras, N. Bergeal, A. Kushwaha, T. Wolf, A. Rastogi, R. C. Budhani, and J. Lesueur, Two-dimensional superconductivity at a Mott insulator/band insulator interface $LaTiO_3/SrTiO_3$, *Nat. Commun.* 1(1), 89 (2010)
18. T. T. Zhang, C. Y. Gu, Z. W. Mao, X. F. Chen, Z. B. Gu, P. Wang, Y. F. Nie, and X. Q. Pan, Mott insulator to metal transition driven by oxygen incorporation in

epitaxial $LaTiO_3$ films, *Appl. Phys. Lett.* 115(26), 261604 (2019)
19. M. J. Veit, M. K. Chan, B. J. Ramshaw, R. Arras, R. Pentcheva, and Y. Suzuki, Three-dimensional character of the Fermi surface in ultrathin $LaTiO_3/SrTiO_3$ heterostructures, *Phys. Rev. B* 99(11), 115126 (2019)
20. J. Biscaras, N. Bergeal, S. Hurand, C. Grossetete, A. Rastogi, R. C. Budhani, D. LeBoeuf, C. Proust, and J. Lesueur, Two-dimensional superconducting phase in $LaTiO_3/SrTiO_3$ heterostructures induced by high-mobility carrier doping, *Phys. Rev. Lett.* 108(24), 247004 (2012)
21. F. D. Wen, Y. W. Cao, X. R. Liu, B. Pal, S. Middey, M. Kareev, and J. Chakhalian, Evolution of ferromagnetism in two-dimensional electron gas of $LaTiO_3/SrTiO_3$, *Appl. Phys. Lett.* 112(12), 122405 (2018)
22. A. Ohtomo, D. A. Muller, J. L. Grazul, and H. Y. Hwang, Artificial charge-modulationin atomic-scale perovskite titanate superlattices, *Nature* 419(6905), 378 (2002)
23. S. Okamoto and A. J. Millis, Electronic reconstruction at an interface between a Mott insulator and a band insulator, *Nature* 428(6983), 630 (2004)
24. S. Okamoto, A. J. Millis, and N. A. Spaldin, Lattice relaxation in oxide heterostructures: $LaTiO_3/SrTiO_3$ superlattices, *Phys. Rev. Lett.* 97(5), 056802 (2006)
25. F. Yang, Z. Z. Wang, Y. H. Liu, S. Yang, Z. Yu, Q. C. An, Z. Q. Ding, F. Q. Meng, Y. W. Cao, Q. H. Zhang, L. Gu, M. Liu, Y. Q. Li, J. D. Guo, and X. R. Liu, Engineered Kondo screening and nonzero Berry phase in $SrTiO_3/LaTiO_3/SrTiO_3$ heterostructures, *Phys. Rev. B* 106(16), 165421 (2022)
26. Y. W. Cao, Z. Z. Yang, M. Kareev, X. R. Liu, D. Meyers, S. Middey, D. Choudhury, P. Shafer, J. D. Guo, J. W. Freeland, E. Arenholz, L. Gu, and J. Chakhalian, Magnetic interactions at the nanoscale in trilayer titanates, *Phys. Rev. Lett.* 116(7), 076802 (2016)
27. H. Y. Hwang, Atomic control of the electronic structure at complex oxide heterointerfaces, *MRS Bull.* 31(1), 28 (2006)
28. Y. Mukunoki, N. Nakagawa, T. Susaki, and H. Y. Hwang, Atomically flat (110) $SrTiO_3$ and heteroepitaxy, *Appl. Phys. Lett.* 86(17), 171908 (2005)
29. A. Annadi, Q. Zhang, X. Renshaw Wang, N. Tuzla, K. Gopinadhan, W. M. Lü, A. Roy Barman, Z. Q. Liu, A. Srivastava, S. Saha, Y. L. Zhao, S. W. Zeng, S. Dhar, E. Olsson, B. Gu, S. Yunoki, S. Maekawa, H. Hilgenkamp, T. Venkatesan, and Ariando, Anisotropic two-dimensional electron gas at the $LaAlO_3/SrTiO_3$ (110) interface, *Nat. Commun.* 4(1), 1838 (2013)
30. Y. L. Han, Y. W. Fang, Z. Z. Yang, C. J. Li, L. He, S. C. Shen, Z. Z. Luo, G. L. Qu, C. M. Xiong, R. F. Dou, X. Wei, L. Gu, C. G. Duan, and J. C. Nie, Reconstruction of electrostatic field at the interface leads to formation of two-dimensional electron gas at multivalent (110) $LaAlO_3/SrTiO_3$ interfaces, *Phys. Rev. B* 92(11), 115304 (2015)
31. Y. Z. Chen, N. Bovet, F. Trier, D. V. Christensen, F. M. Qu, N. H. Andersen, T. Kasama, W. Zhang, R. Giraud, J. Dufouleur, T. S. Jespersen, J. R. Sun, A. Smith, J. Nygard, L. Lu, B. Buchner, B. G. Shen, S. Linderoth, and N. Pryds, A high-mobility two-dimensional electron gas at the spinel/perovskite interface of γ-$Al_2O_3/SrTiO_3$, *Nat. Commun.* 4(1), 1371 (2013)
32. V. F. Gantmakher, Electrons and Disorder in Solids, New York: Oxford University Press, 2005
33. B. L. Altshuler and A. G. Aronov, Modern Problems in Condensed Matter Sciences, New York: Elsevier, 1985, Vol. 10, Ch. 1, pp 1–153
34. S. Das, A. Rastogi, L. J. Wu, J. C. Zheng, Z. Hossain, Y. M. Zhu, and R. C. Budhani, Kondo scattering in δ-doped $LaTiO_3/SrTiO_3$ interfaces: Renormalization by spin–orbit interactions, *Phys. Rev. B* 90(8), 081107(R) (2014)
35. S. Das, Z. Hossain, and R. C. Budhani, Signature of enhanced spin–orbit interaction in the magnetoresistance of $LaTiO_3/SrTiO_3$ interfaces on δ doping, *Phys. Rev. B* 94(11), 115165 (2016)
36. T. A. Costi, A. C. Hewson, and V. Zlatic, Transport coefficients of the Anderson model via the numerical renormalization group, *J. Phys.: Condens. Matter* 6(13), 2519 (1994)
37. D. Goldhaber-Gordon, J. Gores, M. A. Kastner, H. Shtrikman, D. Mahalu, and U. Meirav, From the Kondo regime to the mixed-valence regime in a single-electron transistor, *Phys. Rev. Lett.* 81(23), 5225 (1998)
38. M. Lee, J. R. Williams, S. Zhang, C. D. Frisbie, and D. Goldhaber-Gordon, Electrolyte gate-controlled Kondo effect in $SrTiO_3$, *Phys. Rev. Lett.* 107(25), 256601 (2011)
39. S. Mozaffari, S. Guchhait, and J. T. Markert, Spin–orbit interaction and Kondo scattering at the $PrAlO_3/SrTiO_3$ interface: Effects of oxygen content, *J. Phys.: Condens. Matter* 29(39), 395002 (2017)
40. D. Shoenberg, Magnetic Oscillations in Metals, Cambridge: Cambridge University Press, 2009
41. A. D. Caviglia, S. Gariglio, C. Cancellieri, B. Sacépé, A. Fête, N. Reyren, M. Gabay, A. F. Morpurgo, and J. M. Triscone, Two-dimensional quantum oscillations of the conductance at $LaAlO_3/SrTiO_3$ interfaces, *Phys. Rev. Lett.* 105(23), 236802 (2010)
42. H. Murakawa, M. S. Bahramy, M. Tokunaga, Y. Kohama, C. Bell, Y. Kaneko, N. Nagaosa, H. Y. Hwang, and Y. Tokura, Detection of Berry's phase in a bulk Rashba semiconductor, *Science* 342(6165), 1490 (2013)
43. M. J. Veit, R. Arras, B. J. Ramshaw, R. Pentcheva, and Y. Suzuki, Nonzero Berry phase in quantum oscillations from giant Rashba-type spin splitting in $LaTiO_3/SrTiO_3$ heterostructures, *Nat. Commun.* 9(1), 1458 (2018)
44. M. Ben Shalom, C. W. Tai, Y. Lereah, M. Sachs, E. Levy, D. Rakhmilevitch, A. Palevski, and Y. Dagan, Anisotropic magnetotransport at the $SrTiO_3/LaAlO_3$ interface, *Phys. Rev. B* 80(14), 140403(R) (2009)
45. M. Basletic, J. L. Maurice, C. Carrétéro, G. Herranz, O. Copie, M. Bibes, E. Jacquet, K. Bouzehouane, S. Fusil, and A. Barthélémy, Mapping the spatial distribution of charge carriers in $LaAlO_3/SrTiO_3$ heterostructures, *Nat. Mater.* 7(8), 621 (2008)
46. O. Copie, V. Garcia, C. Bödefeld, C. Carrétéro, M. Bibes, G. Herranz, E. Jacquet, J. L. Maurice, B. Vinter, S. Fusil, K. Bouzehouane, H. Jaffrés, and A. Barthélémy, Towards two-dimensional metallic behavior

at $LaAlO_3/SrTiO_3$ interfaces, *Phys. Rev. Lett.* 102(21), 216804 (2009)
47. J. Q. Xiao, J. S. Jiang, and C. L. Chien, Giant magnetoresistance in nonmultilayer magnetic systems, *Phys. Rev. Lett.* 68(25), 3749 (1992)
48. H. Shin, C. Liu, S. Godin, F. Li, R. Sutarto, B. A. Davidson, and K. Zou, Highly tunable ferromagnetic 2D electron gases at oxide interfaces, *Adv. Mater. Interfaces* 9(32), 2201475 (2022)
49. Y. Ayino, P. Xu, J. Tigre-Lazo, J. Yue, B. Jalan, and V. S. Pribiag, Ferromagnetism and spin-dependent transport at a complex oxide interface, *Phys. Rev. Mater.* 2(3), 231401(R) (2018)
50. A. Schmehl, F. Lichtenberg, H. Bielefeldt, J. Mannhart, and D. G. Schlom, Transport properties of $LaTiO_{3+x}$ films and heterostructures, *Appl. Phys. Lett.* 82(18), 3077 (2003)
51. Z. S. Popovic and S. Satpathy, Wedge-shaped potential and airy-function electron localization in oxide superlattices, *Phys. Rev. Lett.* 94(17), 176805 (2005)